PHOTONICS Research

Monolithic integration of a metalens collimator mosaic on the backside of a light-emitting diode

Yu-Min Chang, Teng-Li Shao, Po-Yang Chang, Yu-Chi Lee, Yu-Kuan Hsieh, Wen-Hsuan Hsieh, Tien-Chang Lu, Yao-Wei Huang, and Chia-Yen Huang*

Department of Photonics, National Yang Ming Chiao Tung University, Hsinchu 30010, Taiwan
**Corresponding author: cyhuang06@nycu.edu.tw*

Received 10 April 2025; revised 17 July 2025; accepted 21 July 2025; posted 23 July 2025 (Doc. ID 564767); published 1 October 2025

A GaN-based metalens collimator (MC) is designed to convert a light-emitting dipole to a plane wave. Finite-difference time-domain (FDTD) simulations show that this structure reduces the far-field divergence angle to below 10°, with the integrated intensity within a 10° escaping cone (I_{10}) enhanced by more than 20 times. However, when random off-focus dipoles are taken into account, the overall enhancement declines significantly. We fabricated MC mosaic partitions of different widths on the backside of an LED epitaxy. Angle-resolved photoluminescence measurements showed that the I_{10} of a 4-μm MC mosaic was 2.84 times higher than that of 8-μm mosaics, and 2-μm mosaics achieved 2.46 times enhancement. We attributed the significant impact of the mosaic dimension to a balance between the effective collimating area relative to the active region and the size-dependent collimating capability.

https://doi.org/10.1364/PRJ.564767

1. INTRODUCTION

The III-nitride micro-light-emitting diode (μ-LED) has been regarded as a strong candidate for next-generation near-eye displays for virtual reality and augmented reality technologies due to its ultra-high pixel density and dynamic range [1–3]. Recently, μ-LEDs have also been considered as the information carrier for co-packaged optics in data communication [4–7]. However, as the gap between pixels shrinks to a few micrometers, the optical crosstalk has been another limiting factor for the overall performance at the module level [8–10]. Therefore, it is critical to reduce the divergence angle (θ_{div}), the angle between the half intensities in spherical coordinates, of the μ-LED by external packaging or integrated nanostructures. The light leaking through the sidewalls might be suppressed by substrate lift-off or filling the gap with light-absorbing materials [11–13]. However, the emission from the top surface is still Lambertian-like with $\theta_{div} \sim 120°$. The fabrication and heterogeneous integration of micro-lens collimator arrays become more and more challenging as the pixel dimension reduces [14–16]. Coupling the emitting dipole to monolithic sub-wavelength structures, for example, photonic crystals [17,18], nano-wires [19], plasmonic arrays [20], or vertical resonant cavities [21,22], has been regarded as a potential approach for beam collimation. However, tailoring the wavefront with nanocavities or metal often sacrifices the output power. Therefore, how to collimate the light out of the μ-LEDs more efficiently is still a critical issue for optical design and photonics science.

In the past decades, metalenses have demonstrated a variety of functionalities from imaging to micro-fabrication [23–26]. Metasurfaces were also monolithically integrated into the surface-emitting lasers to manipulate the beam's properties, such as the far-field pattern (FFP) and angular momentum on the light's exit [27–30]. However, metasurfaces designed for LEDs are much fewer because the photons are generated at random positions with incoherent phases [31–35]. Thus, the phase profile is difficult to formulate for the desired functionality. For example, Khaidarov *et al.* deflected the emission pattern of the red resonant-cavity LED with a metasurface on the distributed Bragg's reflector. However, the function no longer applies without the cavity [33]. Mohtashami *et al.* demonstrated the focusing and beam steering of spontaneous emission by embedding the active region within the meta-atoms [34,35]. The light-emitting metasurface is partly functional with a background intensity since the dipoles are spatially confined. In this study, we demonstrated metalens collimator (MC) mosaic arrays monolithically integrated on the backside of the light-emitting diode epitaxy. By optimizing the dimension of the mosaic partition, the θ_{div} of the FFP can be reduced while the output power along the normal axis is enhanced 2.8 times simultaneously with a uniform dipole emission in the quantum wells. The impact of the mismatches

in dipole position and processing accuracy on the final θ_{div} will also be discussed.

2. DESIGN AND SIMULATION

The physical mechanism of MC is similar to that of conventional micro-lenses, but it is achieved by a two-dimensional (2D) phase profile constructed by discrete sub-wavelength meta-atoms. If a plane wave can be focused by a micro-lens, then the point emission from the focus will be collimated back to a plane wave via inverse propagation, as depicted in Fig. 1(a). The phase difference can be created by the light propagation through meta-atoms with different effective indices and polarization properties. Hence, the 2D phase profiles can be constructed by arranging the meta-atoms representing different phases at different locations.

A typical meta-lens phase profile, $\psi_{lens}(r)$ is deployed on the GaN surface as [24]

$$\psi_{lens}(r) = \frac{2\pi}{\lambda} n_{GaN}\left(F - \sqrt{F^2 + r^2}\right), \quad (1)$$

where n_{GaN} is the refractive index of GaN at a wavelength (λ) of 450 nm ($n_{GaN} = 2.42$), F is the focal length, and r is the radial distance of the meta-atom from the optical axis. The F is set to be 5 μm to simulate the distance between the GaN/sapphire interface and the quantum well (QW) in the commercial LED epitaxy. The constituting meta-atoms for MC are GaN cylinders on GaN with varying diameters (D) and a fixed height (h) in a hexagonal lattice. The hexagonal lattice is chosen due to its privilege in forming wide-angle and high-efficiency metalenses with simple geometry meta-atoms [36]. Other lattices, such as a square lattice or a monoclinic lattice, might have a higher potential for versatile meta-atom geometries with anisotropic polarization manipulation, but the design and fabrication are also more challenging [37,38]. A smaller lattice constant might be preferred for the higher spatial sampling frequency of the phase profile, but it has to be compatible with the established processing capability. The dependence of propagation phase and transmittance on D is calculated by RETICOLO [39]. In this research, D has to be larger than 80 nm and at least 50 nm smaller than the periodicity, and the periodicity has to be sub-wavelength. The maximum aspect ratio of the meta-atom is limited to seven according to the finite selectivity of our hard mask. After optimization in overall transmittance, the periodicity of the array is 360 nm, and h is 450 nm. The meta-atom library with a full 2π phase coverage is summarized in Fig. 1(b). The D ranges from 100 to 275 nm, and the average simulated transmittance is 0.86. The maximum transmittance is limited by the mismatch of the electrical and magnetic dipole responses of the meta-atom [40]. Nearly Huygens metasurfaces might be approached by adopting free-form meta-atoms by inverse design [41]. In this study, we only used the cylinder library to mitigate the complexity of design and fabrication. The characteristics of MC are then verified by finite-difference time-domain (FDTD) simulations by Ansys Lumerical. A dipole source is placed at the focal point, and the 8 μm × 8 μm MC is surrounded by vertical perfectly matched layers (PMLs). The PML is also placed at the bottom of p-GaN to suppress the backside reflection. The simulated FFPs are plotted in Figs. 1(c) and 1(d). In the normalized polar plot, θ_{div} is reduced from 117.2° to 5.0° with the implementation of MC on top. The normal intensity at 0° is enhanced 172 times. The data communication often relies on vertical-cavity surface-emitting lasers (VCSELs), whose θ_{div} is around 15° to 20°. Therefore, we benchmark the integrated power within a 10° escaping cone, I_{10}, which is defined by Eq. (2):

$$I_{10} = \int_{0°}^{10°} I(\theta) 2\pi \sin\theta \, d\theta, \quad (2)$$

where θ is the far-field oblique angle to the normal axis. The I_{10} is enhanced by a factor of 22.8, i.e., $I_{10}^{MC}/I_{10}^{ref} = 22.8$, where I_{10}^{MC} is the measured value with MC and I_{10}^{ref} is the reference value without MC. The enhancement seems to be enormous at first glance. However, if we integrate the power to the entire hemisphere (I_{90}), the enhancement ratio is still less than unity, i.e., $I_{90}^{MC}/I_{90}^{ref} = 0.94$, implying the overall Purcell factor (PF) of the MC is still less than unity. By collecting the optical power from large polar angles toward the optical axis, MC should reduce the optical crosstalk and enhance the normal output power simultaneously.

However, light-emitting dipoles are arbitrarily populated within the QW. Evaluating the overall FFP from numerous incoherent dipoles is challenging for FDTD simulation. We started with surveying the impact of the dipole off-focus and the size of the MC. As illustrated in Fig. 2(a), we assume an 8-μm-square MC with the dipole placed at various lateral positions with off-focus, Δ, along the x direction. Figures 2(b) and 2(c) are the cross-sectional electric field intensity profiles with Δ = 0 μm and 0.4 μm, respectively. When the dipole was placed at the focal points, the spherical wavefront was tailored into a planar one. When the off-focus is relatively small, the tailored wavefront is still planar-like, but the propagation direction deviates from the optical axis, forming an oblique beam in the reverse direction. The simulated top-view FFPs with Δ = 0 μm and 0.4 μm are plotted in Figs. 2(d) and 2(e), respectively. As the Δ is further enhanced, the FFP eventually

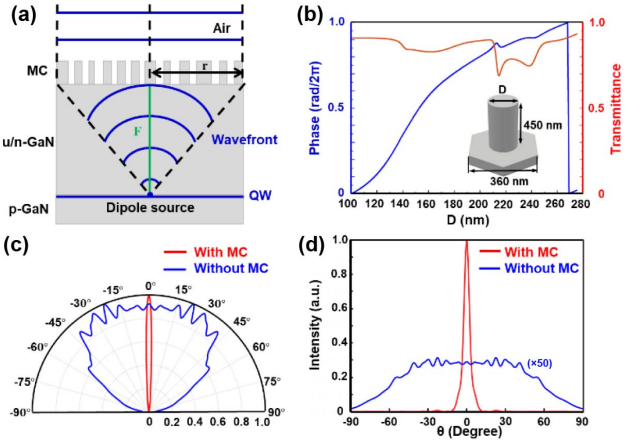

Fig. 1. (a) Schematic of MC to tailor the dipole emission wavefront into a plane wave. (b) The dependence of propagation phase and transmittance on D of the cylindrical meta-atoms. (c) The normalized intensity polar plot; (d) the relative FFP intensity with and without the MC. The one without MC is multiplied by 50 for image clarity.

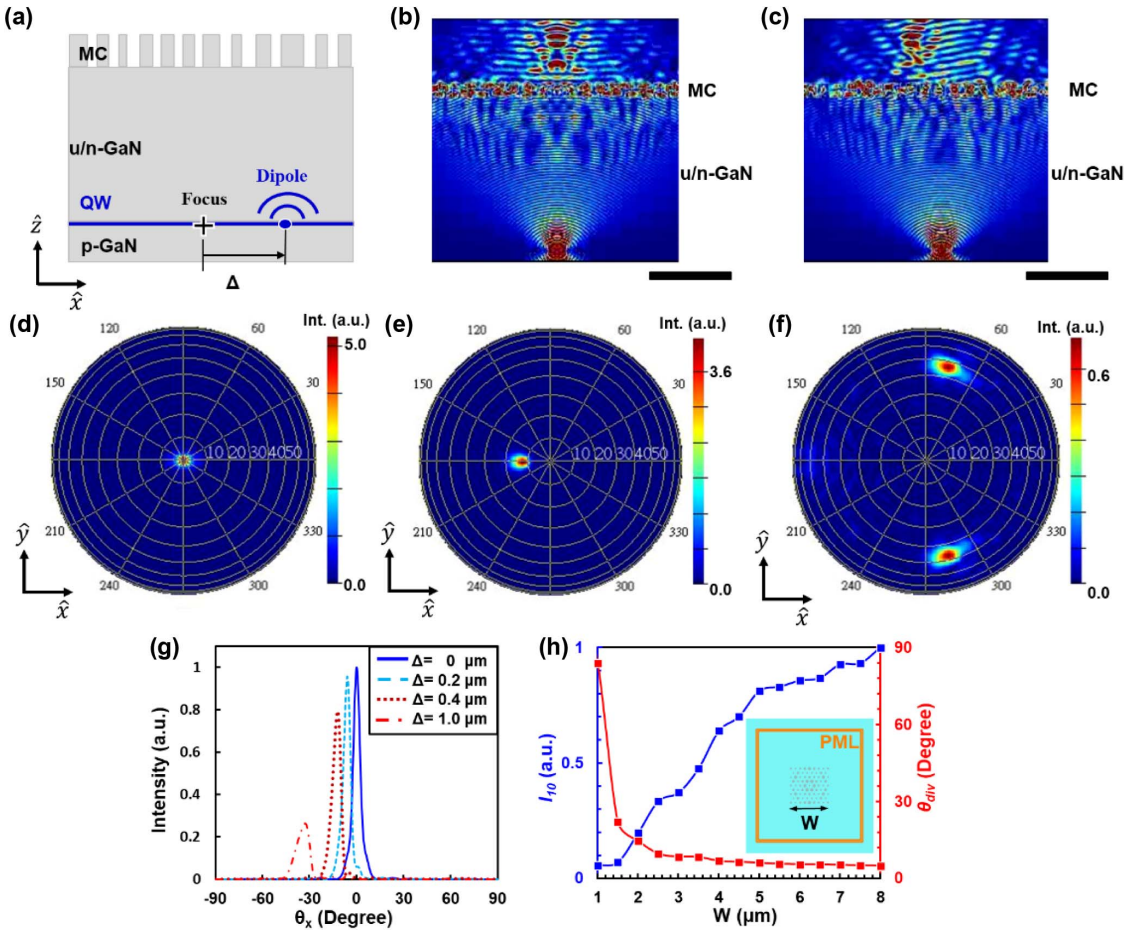

Fig. 2. (a) Schematic structure for a dipole with a lateral off-focus Δ along x direction in the QW normalized cross-sectional electric field intensity plot with (b) $\Delta = 0$ μm and (c) $\Delta = 0.4$ μm. Corner bar represents 2 μm in width. Top view FFPs with (d) $\Delta = 0$ μm, (e) $\Delta = 0.4$ μm, and (f) $\Delta = 2$ μm. (g) FFP intensity on the x – z plane with different Δ, and (h) the dependence of θ_{div} and I_{10} on the width of the square MC, W.

becomes a scattered pattern, as in Fig. 2(f). The simulated FFPs along the polar angle in the x direction are summarized in Fig. 2(g). The interaction between MC and the dipole source with a small Δ resembles the conventional lens imaging in ray optics, but it is in the reverse propagating direction. The larger the Δ, the higher the oblique angle and the weaker the intensity. Here we introduce the concept of effective collimating area, $A_{c,\text{eff}}$, which is defined as follows. When the FFP maximum of a dipole emission through the MC is still within a given θ_{div}, we say the dipole emission is effectively collimated by the MC, and the collection of the dipole positions is the $A_{c,\text{eff}}$. For example, if θ_{div} is assigned to be 20°, then the $A_{c,\text{eff}}$ is a circle with a radius of ∼400 nm according to Figs. 2(e) and 2(g). Dipoles outside the $A_{c,\text{eff}}$ have a minimal contribution to power collimation. For the 8-μm-square MC, $A_{c,\text{eff}}$ is only ∼0.8% of the total area. Therefore, overall collimation is insignificant since the dipoles outside the $A_{c,\text{eff}}$ dominate the FFP.

To enhance the $A_{c,\text{eff}}$ ratio over the total area, we propose to cover the light-emitting area with smaller MC mosaics. We conducted another series of FDTD simulations with square MCs with varying widths, W, from 1 to 8 μm. The PML remained the same 8-μm-wide square, and the dipole source was placed at the focus. The dependence of θ_{div} and I_{10} on W is plotted in Fig. 2(h). θ_{div} increases rapidly when W is less than 2 μm. It can be explained by the minimal interaction of the dipole wavefront with the small MC. When $W > 2$ μm, the MC starts to dominate the FFP, and the θ_{div} gradually decreases with W. The I_{10} increases significantly with W and gradually saturates. Since the contribution to power collimation from the MC margin reduces with W, the gain in power collimation cannot balance the loss from the shrinking $A_{c,\text{eff}}$ ratio after some finite W.

Figures 3(a)–3(c) are three MC mosaic designs with the same total area: single 8-μm-square MC, 4-μm-square, and 2-μm-square MC mosaic partition. The foci are all at the center of each mosaic, marked as "+", with the same F. The $D(r)$ is retrieved from Fig. 1(b) according to the propagation phase profile of Eq. (1). The emitting dipoles were placed at a position with varying Δ along the x direction from the assigned focus in blue. Simulated FFPs with 4-μm-square and 2-μm-square MC mosaic partitions can be found in Figs. 3(d)–3(i). Although the intensity is plotted in an arbitrary unit, the scale is universal among all FFPs. The varying trend of peak position with Δ is consistent with those with the 8-μm-square MC in Figs. 2(c)–2(e), but the peak is weaker and broader with a smaller MC mosaic partition. The overall FFP with uniform

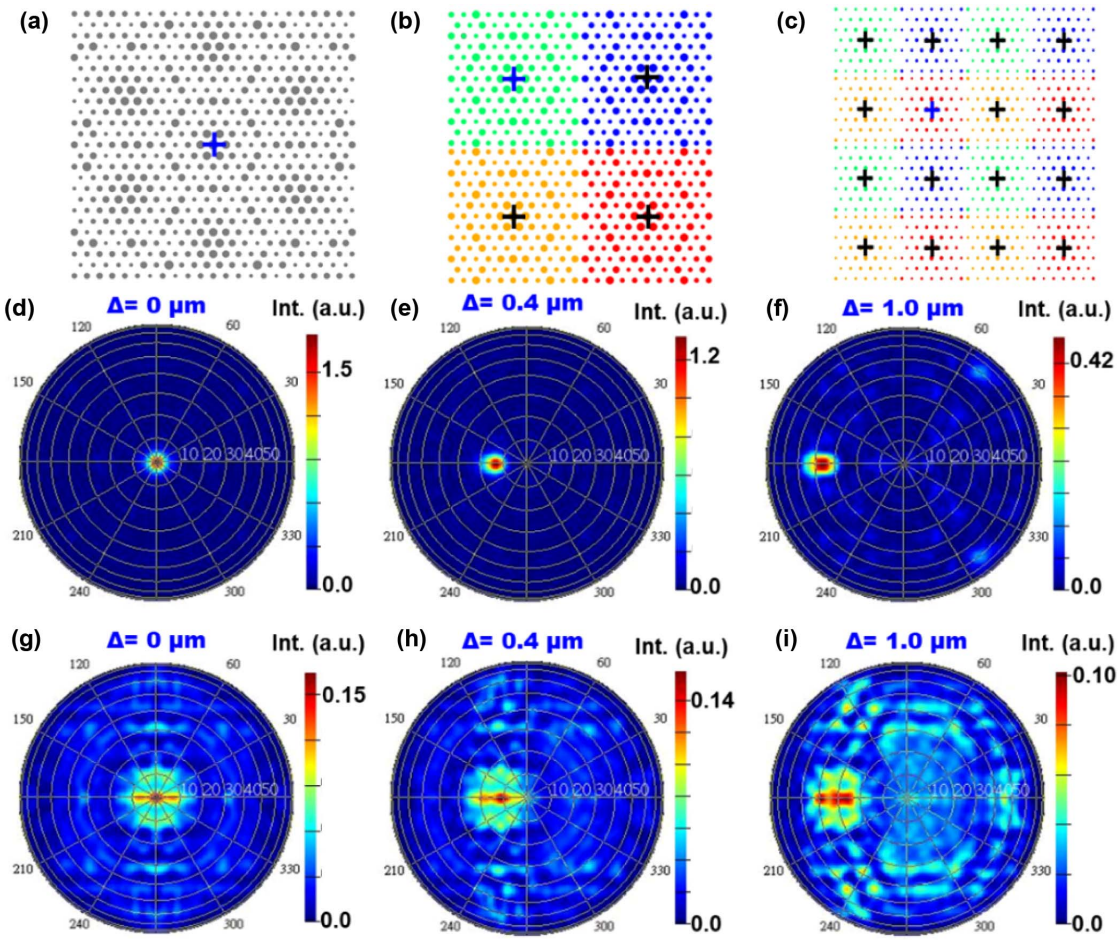

Fig. 3. Schematic MC mosaic pattern with (a) 8 μm, (b) 4 μm, and (c) 2 μm square partition. The "+" in blue is the assigned foci for FFP simulation. The projections of FFP on the $x-y$ plane with $\Delta = 0$ μm, 0.4 μm, and 1 μm are shown in (d)–(f) for 4-μm square partition and in (g)–(i) for 2-μm square partition.

random dipoles is accessed by symmetry operation and dipole statistics. The MC was divided into annular zones with a representing dipole, as depicted in Fig. 4(a). Zone-1 is a 100-nm-radius (r) circle with the dipole at $\Delta = 0$ nm; Zone-2 is an annulus from $r = 100$ nm to $r = 300$ nm with the dipole at $\Delta = 200$ nm, etc. Since the MC phase profile is only a function of r, the FFP of any dipole in the same zone can be acquired by azimuthal rotation of the simulated FFP from the representing dipole. The zone-averaged FFP, $\bar{I}(\theta)$, is then evaluated by Eq. (3):

$$\bar{I}(\theta) = \frac{1}{2\pi}\sum_{i}^{N}\frac{A_i}{A_{\mathrm{MC}}}\int_{0}^{2\pi} I_i(\theta,\varphi)\mathrm{d}\varphi, \tag{3}$$

where $I_i(\theta,\varphi)$ is the simulated FFP of the representing dipole in Zone-i, φ is the azimuthal angle in spherical coordinates, A_i is the area of Zone-i, and A_{MC} is the area of a single mosaic. The A_i/A_{MC} represents the weight of dipoles in Zone-i with a uniform dipole distribution. To sum up all the contributing FFPs to the edge of the mosaic, $N = 5$ is necessary for the 2-μm mosaic, $N = 10$ for the 4-μm mosaic, and $N = 20$ for the 8-μm mosaic. As the W decreases, A_i/A_{MC} increases proportionally to W^{-2}. However, the intensity of $I_i(\theta,\varphi)$ also decreases due to the reduced numerical aperture. There shall be some optimal W for the two competing mechanisms. The calculated polar plots of $\bar{I}(\theta)$ for $W = 8$ μm, 4 μm, and 2 μm are in Fig. 4(b). A distinct peak is presented at $\theta = 0°$ for $W = 4$ μm, and the peak is rounded for $W = 2$ μm due to the scattered FFPs. For the $W = 8$ μm case, the peak intensity occurs at $\theta \sim 45°$, which is contributed by the FFPs from dipoles with $\Delta > 1.6$ μm. Therefore, the sidelobe intensity at $\theta \sim 45°$ is much suppressed for the mosaic with $W = 2$ μm and 4 μm. The integrated power within the 10° escaping cone, $\bar{I}_{10}$, is also calculated in Eq. (2). If we normalize the $\bar{I}_{10}$ with $W = 8$ μm to unity ($\bar{I}_{10}^{8\,\mu\mathrm{m}} = 1$), then $\bar{I}_{10}^{4\,\mu\mathrm{m}} = 3.30$ and $\bar{I}_{10}^{2\,\mu\mathrm{m}} = 3.12$. As a result, $W = 4$ μm is predicted to be the optimal design for the MC mosaic partition. This dimension is also compatible with most μ-LED applications.

3. EXPERIMENTAL RESULTS

A commercial blue LED wafer grown on a (001) flat sapphire substrate (FSS) is bonded to another double-side polished (DSP) sapphire carrier with UV-sensitive glue under i-line

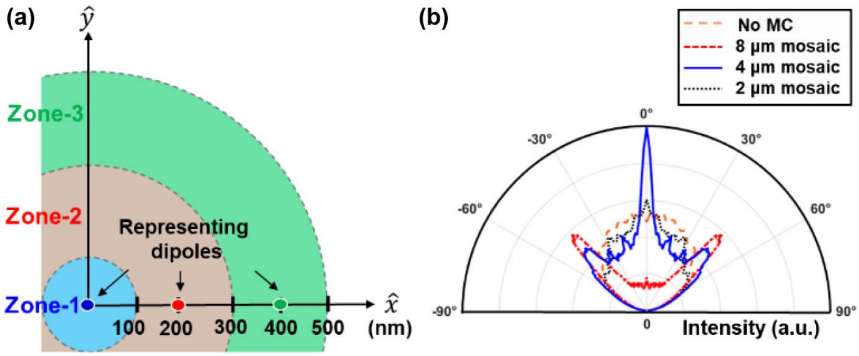

Fig. 4. (a) Schematic of annular zone division centering on the focus and representing dipoles. (b) Calculated zone-averaged FFP up to $N = 5$ for the 2-μm mosaic, $N = 10$ for the 4-μm mosaic, and $N = 20$ for the 8-μm mosaic.

irradiation, as depicted in Fig. 5(a). The distance between the active region and the sapphire substrate is around 5 μm. The FSS substrate was lifted off by a KrF_2 excimer laser, as shown in Fig. 4(b). The sample was immersed in dilute HCl to remove the residual Ga on the surface. A 250-nm-thick SiO_2 is deposited on the N-face of GaN as the hard mask by a plasma-enhanced chemical vapor deposition system. The MC mosaics are patterned on different positions of wafers with negative-tone resist (maN2403) for e-beam lithography (EBL). The patterned area is a 128-μm-wide square with an 8-μm, 4-μm, or 2-μm MC mosaic partition. The schematic cross-sectional profile after EBL is depicted in Fig. 5(c). The pattern was transferred to the SiO_2 hard mask and then GaN by a two-step dry-etching. Finally, the SiO_2 is removed by buffered oxide etchant, as depicted in Fig. 5(d). The area without MC mosaics was covered with 500-nm-thick Cr by a conventional lift-off method to minimize the contribution of photoluminescence (PL) outside the MC mosaics area. Figures 5(e)–5(g) are the top view, bird's-eye view, and cross-sectional view of scanning electron microscopy (SEM) images of the MC mosaic under different magnifications, respectively. Due to the finite-etching selectivity between the oxide hard mask and GaN, the sidewall is ∼15° tilted from verticality.

Figure 6(a) schematically illustrates the angle-resolved PL setup for FFP measurement. The sample was mounted vertically on a triple-axis translational stage. A continuous-wave and collimated 405-nm laser beam is irradiated from the DSP sapphire end for excitation. The beam size after the iris is expected to be around 400 μm, which is larger than the span of the MC mosaics. Therefore, we can assume a uniform excitation of the dipoles in the MQW region. A long-pass filter with a 425-nm cutoff wavelength and a fiber coupler are mounted on a motorized rotational arm toward the sample. The fiber coupler was connected to a spectrometer for the PL spectrum. The FFP is measured by the PL intensity at 450 nm from different angles.

The polar plots of FFP and their normalized plot are shown in Figs. 6(b) and 6(c), respectively. In general, the FFP with

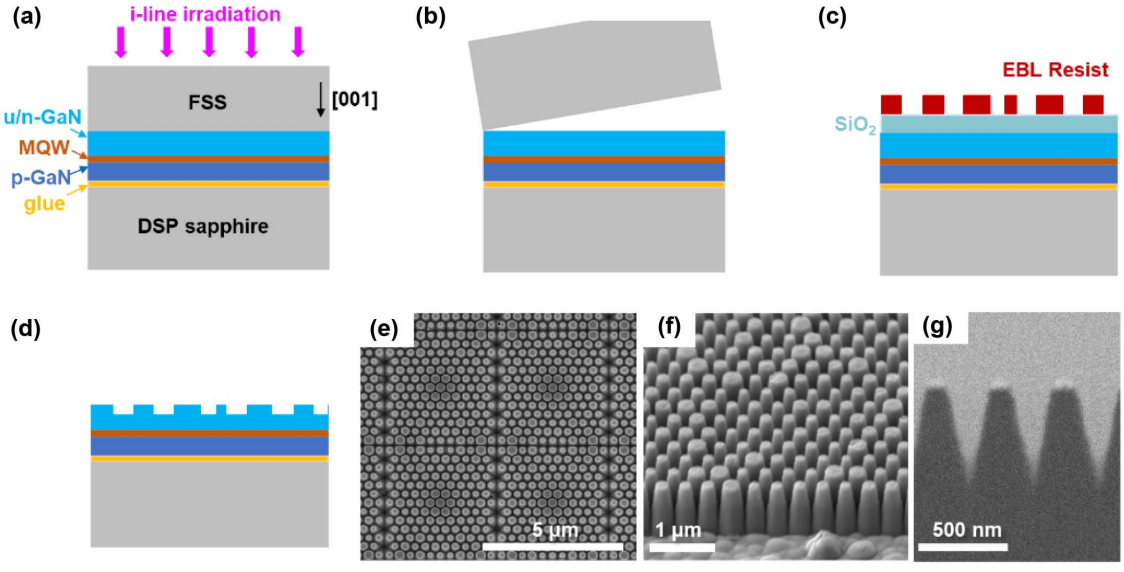

Fig. 5. Schematic cross-section profile when (a) the LED wafer is bonded to DSP sapphire with UV-sensitive glue; (b) the substrate is lifted off by KrF_2 excimer laser; (c) the MC is patterned via EBL; and (d) the MC pattern is transferred to GaN via etching and then BOE immersion. The (e) top-view, (f) bird's-eye-view, and (g) cross-sectional SEM images of MC.

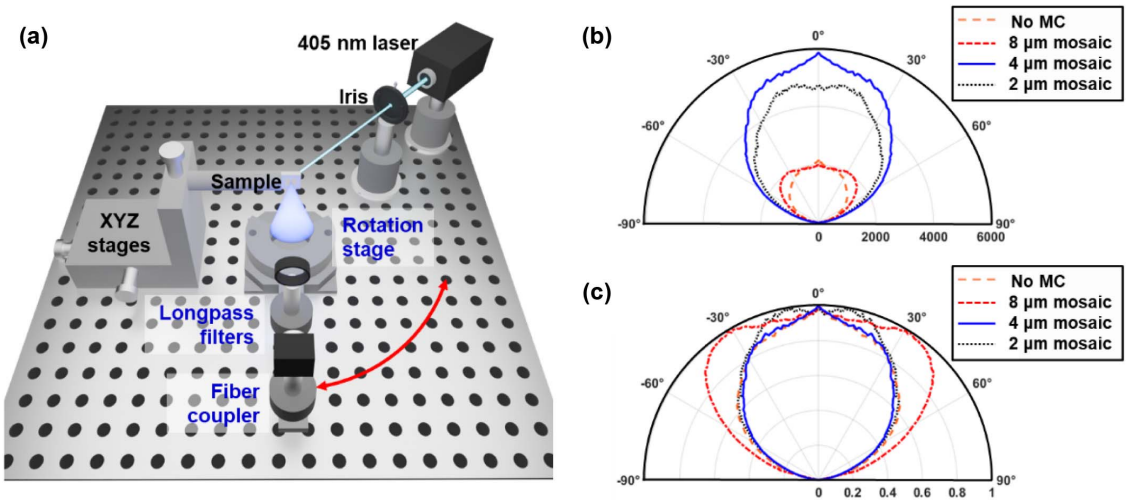

Fig. 6. (a) Schematic angle-resolved PL setup for FFP; (b) the raw and (c) normalized FFP polar plot with and without MC mosaics.

a higher intensity at $\theta = 0°$ also possesses a lower θ_{div}. The corresponding θ_{div} is 116°, 132°, 108°, and 112° for the area without MC, and with 8-μm, 4-μm, and 2-μm MC mosaics, respectively. The overall θ_{div} is still broad since the active region is uniformly excited. The maximum $A_{c,eff}$ ratio is still ~12% for the 2-μm MC mosaics. If we normalize the I_{10} with the 8-μm MC mosaic to be one, those with 4-μm and 2-μm MC mosaics are 2.84 and 2.46, respectively. The FFP shows $\theta \sim 0°$ is the strongest for the 4-μm MC mosaics, and that with the 2-μm MC mosaic is more rounded, which is consistent with the simulated FFP in Fig. 4(b). The qualitative agreement of the I_{10} order validated the effectiveness of our simulation. The quantitative discrepancy might be attributed to various root causes, for example, the meta-atom geometry and the epitaxial structure mismatch between experiments and simulations. For example, we studied the impact of the 15° sidewall inclination with the same meta-atom top diameter by optical simulations. Figure 7(a) summarizes the dependence of the propagation phase and transmittance of the 450-nm-high cylindrical meta-atoms with a 15°-tilted sidewall. The propagation phases deviated from those with vertical sidewalls, but the difference does not vary drastically with D. Therefore, we can expect the actual phase with the tilted sidewalls to be close to the original metalens collimator. Figure 7(b) shows the θ_{div} only deteriorated from 5° to 6°, and the I_{10} degraded by 10% if the MC is composed of meta-toms with tilted sidewalls. As long

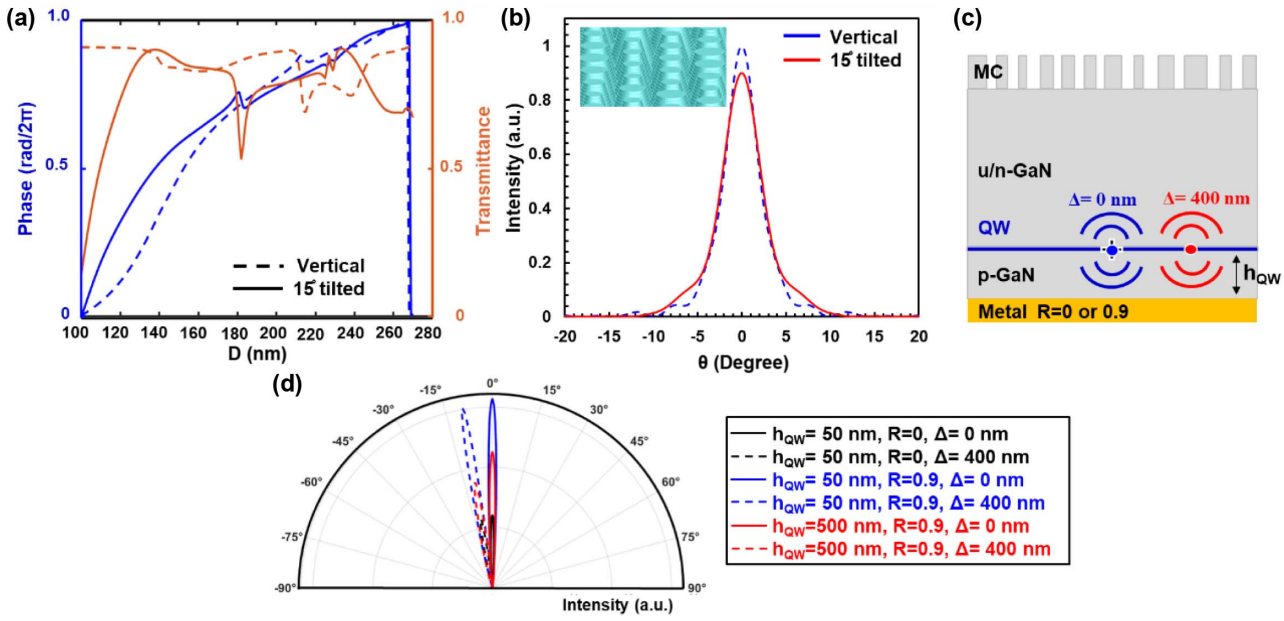

Fig. 7. (a) Dependence of propagation phase and transmittance on the top diameter, D, of the cylindrical meta-atoms with a 15°-tilted (solid line) or vertical (dashed line) sidewall. (b) Simulated FFPs with vertical (blue) and tilted (red) sidewalls with the same $D(r)$ at the top. Inset is the bird's-eye view of MC with 15°-tilted sidewalls in simulation software. (c) Schematic of FDTD simulation considering the backside reflector. (d) Simulated FFPs with different h_{QW}, R, and Δ.

as the imperfection in the process does not change the dependence of the propagation phase on the top diameter significantly, the MC function could still be retained. Besides the continuous refinement in processing accuracy, the performance of MC mosaics could be significantly improved by the following strategies. First, change the mosaic unit from square to hexagon for the closest packing of the $A_{c,\mathrm{eff}}$. Second, concentrate the light-emitting dipoles in the $A_{c,\mathrm{eff}}$ by selective area micro-PL excitation or current injection. If all the dipoles are spatially constrained in the $A_{c,\mathrm{eff}}$, the light shall be well-collimated within the θ_{div}. Third, we could also modify the phase profiles of the MC to optimize the $A_{c,\mathrm{eff}}$. More elaborate simulation-assisted design optimization and processing development will be further investigated.

In real micro-LED devices, the bottom metal contact could have a strong impact on the light collimation. First, carriers could be selectively injected by the pad design to manipulate the FFP. Second, the output power will be enhanced if the metal is highly reflective. Figure 7(c) illustrates the schematic of the simulations considering different backside metal reflectance ($R = 0\%$ or $R = 90\%$), the distance between the QW and the metal ($h_{\mathrm{QW}} = 50$ nm or $h_{\mathrm{QW}} = 500$ nm), and the dipole position at $\Delta = 0$ nm or $\Delta = 400$ nm. The simulated FFPs with the 8-μm mosaic are shown in Fig. 7(d). In general, the dependence of oblique angle on Δ is similar after inclusion of the back reflector. The FFP intensity will be higher if the reflector is close to the QW. Finally, since the MC is designed to interact with the dipole emission propagating along the normal axis, the sidewalls of micro-LEDs are expected to contribute to the parasitic background in the FFP, which might be suppressed by filling the gaps with light-absorbing materials.

4. CONCLUSION

In conclusion, we designed and demonstrated the monolithically integrated MC on the backside of the LED epitaxy. A wide MC collimates the dipole emission in the focus vicinity more efficiently, but the effective area will be insignificant to the total light-emitting area. Therefore, the LED backside area has an optimized partition for the MC mosaic. For the conventional blue LED epi with the active region ~5 μm from the GaN/sapphire interface, the normal output power can be enhanced up to 2.8 times with a reduced divergence angle after incorporating the 4-μm MC mosaics on the backside. The divergence angle could be further suppressed by etching the active region away from the focus or selectively injecting the carriers via electrode pattern design in the real μ-LED. The MC mosaic integration with thin-film LED epitaxy provides an ultra-compact solution to suppress the optical cross-talk of high-density μ-LED arrays for future near-eye displays and co-packaged optics modules.

Funding. National Science and Technology Council (NTSC-113-2628-E-A49-008).

Acknowledgment. This work was financially supported by the National Science and Technology Council (NTSC) of Taiwan. The authors thank the best Epitaxy Manufacturing Ltd., Taiwan, for supporting the blue LED epitaxial wafer and laser lift-off.

Disclosures. The authors have no conflicts of interest.

Data Availability. Data underlying the results presented in this paper are not publicly available at this time but may be obtained from the authors upon reasonable request.

REFERENCES

1. A. R. Anwar, M. T. Sajjad, M. A. Johar, *et al.*, "Recent progress in micro-LED-based display technologies," Laser Photonics Rev. **16**, 2100427 (2022).
2. Y. Huang, E. Hsiang, M. Deng, *et al.*, "Mini-LED, micro-LED and OLED displays: present status and future perspectives," Light Sci. Appl. **9**, 105 (2020).
3. W. Miao, F. Hsiao, Y. Sheng, *et al.*, "Microdisplays: mini-LED, micro-OLED, and micro-LED," Adv. Opt. Mater. **12**, 2300112 (2023).
4. W. Tian, H. Hou, H. Dang, *et al.*, "Progress in research on co-packaged optics," Micromachines **15**, 1211 (2024).
5. Z. Li, L. Yu, B. Liu, *et al.*, "High-speed micro-LEDs based on nano-engineered InGaN active region towards chip-to-chip interconnections," J. Lightwave Technol. **42**, 8760–8770 (2024).
6. G. Lin, H. Kuo, C. Cheng, *et al.*, "Ultrafast 2 × 2 green micro-LED array for optical wireless communication beyond 5 Gbit/s," Photonics Res. **9**, 2077–2087 (2021).
7. Y. Chang, Y. Huang, F. Liou, *et al.*, "2.805 Gbit/s high-bandwidth phosphor white light visible light communication utilizing an InGaN/GaN semipolar blue micro-LED," Opt. Express **30**, 16938–16946 (2022).
8. L. Qi, X. Zhang, W. Chong, *et al.*, "848 ppi high-bright active-matrix micro-LED micro-display using GaN-on-Si epi-wafers towards mass production," Opt. Express **29**, 10580–10591 (2021).
9. Y. Xu, J. Cui, Z. Hu, *et al.*, "Pixel crosstalk in naked-eye micro-LED 3D display," Appl. Opt. **60**, 5977–5983 (2021).
10. K. Li, Y. Cheung, C. Tang, *et al.*, "Optical crosstalk analysis of micro-pixelated GaN-based light-emitting diodes on sapphire and Si substrates," Phys. Status Solidi A **213**, 1193–1198 (2016).
11. F. Gou, E. Hsiang, G. Tan, *et al.*, "Angular color shift of micro-LED displays," Opt. Express **27**, A746–A757 (2019).
12. Y. Yin, Z. Hu, M. U. Ali, *et al.*, "Alleviating the crosstalk effect via a fine-moulded light-blocking matrix for colour-converted micro-LED display with a 122% NTSC gamut," Light Adv. Manuf. **3**, 36 (2022).
13. H. Lin, C. Sher, D. Hsieh, *et al.*, "Optical cross-talk reduction in a quantum-dot-based full-color micro-light-emitting-diode display by a lithographic-fabricated photoresist mold," Photonics Res. **5**, 411–416 (2017).
14. H. W. Choi, C. Liu, E. Gu, *et al.*, "GaN micro-light-emitting diode arrays with monolithically integrated sapphire microlenses," Appl. Phys. Lett. **84**, 2253–2255 (2004).
15. S. Zhang, S. Chen, L. Zhang, *et al.*, "Design and optimization of a collimating lens for ultra-small μLED displays using FDTD simulation," Opt. Express **32**, 46021–46032 (2024).
16. C. Wang, Y. Fan, B. Wang, *et al.*, "Fully enclosed composite micro/nano-package for high-quality micro-LED display pixels and *in situ* nanoimprint technology," Adv. Mater. Technol. **9**, 2301782 (2024).
17. E. Moreno, F. J. Garcia-Vidal, and L. Martin-Moreno, "Enhanced transmission and beaming of light via photonic crystal surface modes," Phys. Rev. B **69**, 121402 (2004).
18. K. Wang, X. Dong, Y. Bu, *et al.*, "Design of photonic crystals for light-emitting diodes," J. Am. Ceram. Soc. **106**, 7146–7188 (2023).
19. M. Kuo, Y. Kim, M. Hsieh, *et al.*, "Efficient and directed nano-LED emission by a complete elimination of transverse-electric guided modes," Nano Lett. **11**, 476–481 (2011).
20. G. Lozano, D. J. Louwers, S. R. Rodriguez, *et al.*, "Plasmonics for solid-state lighting: enhanced excitation and directional emission of highly efficient light sources," Light Sci. Appl. **2**, e66 (2013).

21. J. Huang, M. Tang, B. Zhou, *et al.*, "GaN-based resonant cavity micro-LEDs for AR application," Appl. Phys. Lett. **121**, 201104 (2022).
22. Z. Y. Ooi, A. Jiménez-Solano, K. Gałkowski, *et al.*, "Strong angular and spectral narrowing of electroluminescence in an integrated Tamm-plasmon-driven halide perovskite LED," Nat. Commun. **15**, 5802 (2024).
23. S. Wang, P. Wu, V. Su, *et al.*, "A broadband achromatic metalens in the visible," Nat. Nanotechnol. **13**, 227–232 (2018).
24. M. Khorasaninejad and F. Capasso, "Metalenses: versatile multifunctional photonic components," Science **358**, eaam8100 (2017).
25. X. Zang, H. Ding, Y. Intaravanne, *et al.*, "A multi-foci metalens with polarization-rotated focal points," Laser Photonics Rev. **13**, 1900182 (2019).
26. Y. Peng, Y. Wang, K. Chen, *et al.*, "Deep-ultraviolet AlN metalens with imaging and ultrafast laser microfabrication applications," Nano Lett. **25**, 3141–3149 (2025).
27. Y. Xie, P. Ni, Q. Wang, *et al.*, "Metasurface-integrated vertical cavity surface-emitting lasers for programmable directional lasing emissions," Nat. Nanotechnol. **15**, 125–130 (2020).
28. X. Jia, J. Kapraun, J. Wang, *et al.*, "Metasurface reflector enables room-temperature circularly polarized emission from VCSEL," Optica **10**, 1093–1099 (2023).
29. P. Fu, P. Ni, B. Wu, *et al.*, "Metasurface enabled on-chip generation and manipulation of vector beams from vertical cavity surface-emitting lasers," Adv. Mater. **35**, 2204286 (2023).
30. D. Wen, J. Meng, J. J. Cadusch, *et al.*, "VCSELs with on-facet metasurfaces for polarization state generation and detection," Adv. Opt. Mater. **9**, 2001780 (2021).
31. X. Zeng, H. Hou, Y. Li, *et al.*, "Recent progress of metasurfaces in light-emitting diodes," Appl. Phys. Rev. **11**, 021339 (2024).
32. E. Chen, Z. Fan, K. Zhang, *et al.*, "Broadband beam collimation metasurface for full-color micro-LED displays," Opt. Express **32**, 10252–10264 (2024).
33. E. Khaidarov, Z. Liu, R. Paniagua-Domínguez, *et al.*, "Control of LED emission with functional dielectric metasurfaces," Laser Photonics Rev. **14**, 1900235 (2020).
34. Y. Mohtashami, L. K. Heki, M. S. Wong, *et al.*, "Metasurface light-emitting diodes with directional and focused emission," Nano Lett. **23**, 10505–10511 (2023).
35. Y. Mohtashami, R. A. DeCrescent, L. K. Heki, *et al.*, "Light-emitting metalenses and meta-axicons for focusing and beaming of spontaneous emission," Nat. Commun. **12**, 3591 (2021).
36. C.-Y. Fan, C.-P. Lin, and G.-D. J. Su, "Ultrawide-angle and high-efficiency metalens in hexagonal arrangement," Sci. Rep. **10**, 15677 (2020).
37. S. Kim, J. Kim, K. Kim, *et al.*, "Anti-aliased metasurfaces beyond the Nyquist limit," Nat. Commun. **16**, 411 (2025).
38. S. S. Kruk, A. N. Poddubny, D. A. Powell, *et al.*, "Polarization properties of optical metasurfaces of different symmetries," Phys. Rev. B **91**, 195401 (2015).
39. J. P. Hugonin and P. Lalanne, "RETICOLO software for grating analysis," arXiv, arXiv:2101.00901 (2025).
40. M. Decker, I. Staude, M. Falkner, *et al.*, "High-efficiency dielectric Huygens' surfaces," Adv. Opt. Mater. **3**, 813–820 (2015).
41. P. Dainese, L. Marra, D. Cassara, *et al.*, "Shape optimization for high efficiency metasurfaces: theory and implementation," Light Sci. Appl. **13**, 300 (2024).